



**OPTICS, IMAGE SCIENCE, AND VISION** 

# Accuracy of the multilayer Born approximation in transmission and reflection

PATRICK C. CHAUMET,\* D GUILLAUME MAIRE, AND ANNE SENTENAC

Aix Marseille Univ, CNRS, Centrale Med, Institut Fresnel, Marseille, France \*patrick.chaumet@fresnel.fr

Received 22 November 2024; revised 14 February 2025; accepted 14 February 2025; posted 19 February 2025; published 14 March 2025

The simulation of light scattering by heterogeneous dielectric objects that are large compared to the wavelength is the bottleneck of many quantitative imaging techniques. The rigorous Maxwell equation solvers are slow and have high memory requirements; several approximate models have been developed to address this issue. Most of these models have proved effective in simulating the forward scattered field. In this work, we focus on the multilayer Born (MLB) approximation that has been introduced recently to simulate the backward scattered field. We compare its results to those of a rigorous Maxwell solver. We define a domain of object size and permittivity contrast for which MLB can be used with good accuracy. We point out the superiority of MLB compared to most approximate methods for calculating the backward scattered field. © 2025 Optica Publishing Group. All rights, including for text and data mining (TDM), Artificial Intelligence (Al) training, and similar technologies, are reserved.

https://doi.org/10.1364/JOSAA.549504

### 1. INTRODUCTION

Fast and efficient approximate methods able to simulate light scattering by objects in the microscopic range are of prime importance in numerous domains, such as photonic component design or quantitative imaging [1,2]. In computational microscopy, for example, one recovers the three-dimensional permittivity map of the object from far-field measurements using an inversion procedure. When the object is large or contrasted enough to modify the illumination at the wavelength scale, the inversion procedure becomes iterative and necessitates simulating the light scattering by many successive estimations of the object [3–5]. These simulations, when performed with a rigorous Maxwell solver, are slow and computationally demanding. They limit the application domain of quantitative imaging to relatively small and weakly contrasted samples. Therefore, it is crucial to develop fast simulation tools based on approximate models that are able to consider large samples supporting some multiple scattering [6,7].

Recently, we have compared the performances of different approximate methods, such as the Born approximation, the Rytov approximation [8–10], and the beam propagation method [4,11,12], with a rigorous Maxwell solver, the discrete dipole approximation (DDA) [13], for simulating the scattered field by inhomogeneous dielectric samples of moderate contrast but large size (more than  $10^4\lambda^3$ ) [14]. It was shown that the beam propagation method (BPM) was the most accurate for simulating the field transmitted by the sample [14].

On the other hand, approximate methods able to simulate the field that is back-scattered by dielectric inhomogeneous samples

are still lacking. Indeed, when considering large, weakly contrasted samples, such as cells, the reflected signal is quite weak compared to the transmitted signal. An approximate method, such as the BPM, can provide an accurate transmitted field but a poor estimation of the reflected field [14]. Now, there exist several important computational imaging techniques, such as smart optical coherence tomography [15] or reflection tomography [16–19], that would benefit from scattering models adapted to the reflection geometry.

In this work, we improve a recent approximate technique, the multilayer Born (MLB) approximation [20,21], which seems better adapted to the reflection configuration. We analyze its accuracy on large dielectric samples. Due to rigorous simulations obtained with the DDA, we draw its domain of validity in terms of dielectric contrast and size of the samples. We show that MLB is not as efficient as BPM in transmission but is more accurate for simulating the reflected field even in the presence of some multiple scattering.

### 2. THEORY

In Ref. [20], the multilayer Born approximation was presented in its scalar version. To describe the principle of MLB, we first recall the main steps of the discrete dipole approximation, as both techniques are based on the same concept of dipole radiation.

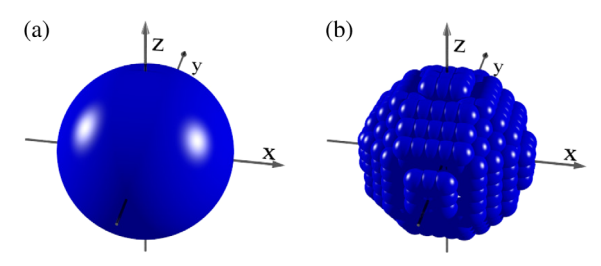


**Fig. 1.** (a) Object under study. (b) Discretization of the object for the DDA. The object is therefore seen as a set of small identical spheres on a cubic mesh of grid spacing *d*.

# A. Principle of the DDA

The DDA is a well-known rigorous method able to simulate the field that takes place inside an object of arbitrary shape and permittivity [13,22–24] when the latter is illuminated by an incident field  $\mathbf{E}_0$ . More precisely, DDA solves the volume-integral equation stemming from Maxwell's equations:

$$\mathbf{E}(\mathbf{r}) = \mathbf{E}_0(\mathbf{r}) + \int_V \mathbf{G}(\mathbf{r}, \mathbf{r}') \chi(\mathbf{r}') \mathbf{E}(\mathbf{r}') d\mathbf{r}', \tag{1}$$

where  $\chi = (\varepsilon - 1)/(4\pi)$  represents the (inhomogeneous) linear susceptibility of the sample, and **G** is the free-space Green's tensor [25].

Once the field  ${\bf E}$  is known in the domain V where  $\chi$  is nonzero (inside the sample), then Eq. (1) can be used to calculate the field everywhere. The simplest approximation, known as the Born approximation (which is valid for weakly contrasted and small enough samples), consists of assuming that the field inside the sample is close to  ${\bf E}_0$ . In this case, the integral of Eq. (1) can be readily calculated to yield the scattered field  $({\bf E}-{\bf E}_0)$  everywhere outside the sample.

When the Born approximation is not valid, one needs to calculate  ${\bf E}$  inside V. To this aim, V is discretized into a set of cubic subunits of size d that are small enough for ensuring that the field and susceptibility are (almost) constant over them (Fig. 1). Then, the macroscopic field at the position of each subunit can be expressed as

$$\mathbf{E}(\mathbf{r}_i) = \mathbf{E}_0(\mathbf{r}_i) + \sum_{j=1, i \neq j}^{N} \mathbf{G}(\mathbf{r}_i, \mathbf{r}_j) d^3 \chi(\mathbf{r}_j) \mathbf{E}(\mathbf{r}_j) - \frac{\varepsilon(\mathbf{r}_i) - 1}{3} \mathbf{E}(\mathbf{r}_i),$$

where *N* is the number of subunits discretizing the object. Note that Eq. (2) is an approximation that holds when the size of the subunit tends toward zero [26]. There are other approaches where the finite size of the subunit is taken into account [23,27].

The field inside the object is obtained by solving the system of linear equations, Eq. (2). In practice, this is done using an iterative method; see Refs. [23,28,29]. Hereafter, all the rigorous simulations of field–object interaction were carried out using our open-source code IFDDA, which enables DDA to be used in a user-friendly way through a graphical user interface [30]. We have set the tolerance threshold for the iterative linear-system-solving method at  $10^{-6}$  to ensure the accuracy of the results.

Another, equivalent, way to write the DDA [31] is to gather all terms dependent on i together. Then, Eq. (2) can be written as

$$\mathbf{E}(\mathbf{r}_i) \frac{\varepsilon(\mathbf{r}_i) + 2}{3} = \mathbf{E}_0(\mathbf{r}_i) + \sum_{j=1, i \neq j}^{N} \mathbf{G}(\mathbf{r}_i, \mathbf{r}_j) d^3 \frac{\varepsilon(\mathbf{r}_j) - 1}{4\pi} \mathbf{E}(\mathbf{r}_j),$$
(3)

where  $\mathbf{E}_{loc} = \frac{\varepsilon + 2}{3}\mathbf{E}$  corresponds to the local field, whereas we recall that  $\mathbf{E}$  corresponds to the macroscopic field. We obtain

$$\mathbf{E}_{\text{loc}}(\mathbf{r}_i) = \mathbf{E}_0(\mathbf{r}_i) + \sum_{j=1, i \neq j}^{N} \mathbf{G}(\mathbf{r}_i, \mathbf{r}_j) \alpha_0(\mathbf{r}_j) \mathbf{E}_{\text{loc}}(\mathbf{r}_j), \quad (4)$$

where  $\alpha_0$  is the polarizability, and  $\alpha_0 = \frac{3}{4\pi} \frac{(\varepsilon-1)}{(\varepsilon+2)} d^3$  denotes the Clausius–Mossotti relationship. In the DDA approach, the object illuminated by  $\mathbf{E}_0$  can be seen as a collection of small spheres of volume  $d^3$  on a cubic mesh of grid spacing d that interact with each other through their dipole moment  $\alpha_0 \mathbf{E}$  [23,32]. In this framework, the Born approximation applies to the local field,  $\mathbf{E}_{\text{loc}} = \mathbf{E}_0$ , and it yields a macroscopic field inside the object equal to  $\mathbf{E} = \frac{3}{\varepsilon+2} \mathbf{E}_0$ . Thus, it takes into account the depolarization phenomenon that reduces the electric field in small spheres compared to the wavelength of illumination. We recall that the electric field inside a sphere plunged in a static field  $\mathbf{E}_0$  is equal to  $\frac{3}{\varepsilon+2} \mathbf{E}_0$  [25]. Then, we have observed empirically that it was more accurate than the classical Born approximation for weakly contrasted samples of any shape, such as those encountered in microscopy applications [33].

Once the field inside the object is known, we calculate the diffracted field **e** in the far field defined in the direction  $\mathbf{k} = k_0 \mathbf{r}/r$  as  $\mathbf{E}(\mathbf{r}) - \mathbf{E}_0(\mathbf{r}) \approx \mathbf{e}(\mathbf{k}) e^{ik_0 r}/r$ . Then all the scattered fields in the **k** directions can be obtained through [34]

$$\mathbf{e}(\mathbf{k}) = \left[k_0^2 \mathbf{I} - \mathbf{k} \otimes \mathbf{k}\right] \int \mathcal{F}_{2D}[\chi \mathbf{E}] e^{ik_z z} dz,$$
 (5)

where  $\mathcal{F}_{2D}$  is the two-dimensional Fourier transform in the (x, y) plane, and  $k_z$  is the z component of  $\mathbf{k}$ . The integration over z is done over the height of the object. In practice, the expression is computed with a two-dimensional fast Fourier transform (FFT) in the (x, y) plane and a Riemann sum along z.

It is worth noting that the scattered far-field could also be calculated by propagating in free space the field obtained at the last layer of the object. With a rigorous Maxwell solver, the two techniques would yield the same result. On the other hand, when the internal field is obtained with an approximate method (BPM, Rytov), the radiation of the induced polarization inside the sample, Eq. (5), yields a significantly better result than free-space propagation from the last layer [14].

### 3. MULTILAYER BORN APPROXIMATION

# A. Principle of Scalar MLB in Transmission

The multilayer Born (MLB) approximation has been introduced recently in the framework of the scalar approximation [20], i.e.,  $\mathbf{G}(\mathbf{r}, \mathbf{r}') = k_0^2 \frac{e^{ikR}}{R} \mathbf{I}$  with  $R = |\mathbf{r} - \mathbf{r}'|$ , which is valid when the permittivity varies on a scale much larger than the wavelength [35]. In this section, we introduce the MLB in a practical way that is ready for a numerical implementation. As in DDA, the object, described by its inhomogeneous susceptibility  $\chi$ , is discretized into subunits (usually due to a cubic mesh) over

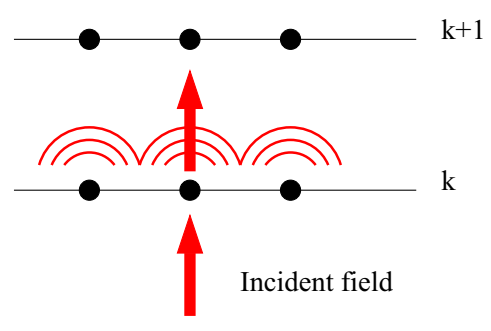


**Fig. 2.** Sketch of the MLB. An incident field impinging on layer k, and the field at layer k + 1 is the sum of the incident field propagated from layer k to k + 1 and the field radiated by the elements of layer k.

which the susceptibility and field are assumed to be constant. We assume that the sample is illuminated by a beam propagating toward positive z and that the field inside the sample is also propagating along positive z. Then we observe that the object is made of K layers of subunits along z ( $k = 1, \dots, K$  with  $z_{k+1} > z_k$ ). The principle of MLB (like BPM) is to assume that the field in layer k + 1 depends only on the field in layer k. It is worth noting that there is a complete equivalence between the MLB and the beam propagation method when the susceptibility  $\chi$  is small, as demonstrated in Appendix B. In the transmission configuration, the field is estimated layer by layer starting from layer 1. The fields inside each layer are noted  $E^k$ . In layer 1,  $E^1$  is taken as the incident field. Then the field inside the layer k + 1 will be the sum of the field at layer k that has undergone free-space propagation from  $z_k$  to  $z_{k+1}$  and the field radiated toward the positive z by the induced polarization in layer k due to  $E^k$ ; see Fig. 2. The relationship between  $E^{k+1}$  and  $E^k$  reads

$$E^{k+1}(\boldsymbol{\rho}_{i}, z_{k+1}) = FFT_{2D}^{-1} \left[ e^{ik_{z}d} FFT_{2D} [E^{k}(z_{k})] \right] (\boldsymbol{\rho}_{i})$$

$$+ \sum_{j} G(\boldsymbol{\rho}_{i}, z_{k+1}, \boldsymbol{\rho}_{j}, z_{k}) \chi(\boldsymbol{\rho}_{j}, z_{k}) d^{3} E^{k}(\boldsymbol{\rho}_{j}, z_{k}),$$
(6)

where  $\mathbf{r} = (\boldsymbol{\rho}, z), k_z > 0$  is the z component of the wave vectors used in the free-space propagation by plane wave expansion, k is the layer number, and (i, j) the number of subunit in the layer k.

# **B. MLB with the Renormalized Born Approximation**

A simple way to improve the accuracy of MLB is to use the renormalized Born approximation, i.e., the polarization of each discretization element of the object, which is expressed as  $\chi d^3$  in Eq. (2), is replaced by the expression  $\alpha$  as shown in Eq. (4). This allows us to rewrite Eq. (6) as

$$E^{k+1}(\boldsymbol{\rho}_{i}, z_{k+1}) = \text{FFT}_{2D}^{-1} \left[ e^{ik_{z}d} \text{FFT}_{2D} [E^{k}(z_{k})] \right] (\boldsymbol{\rho}_{i})$$

$$+ \sum_{j} G(\boldsymbol{\rho}_{i}, z_{k+1}, \boldsymbol{\rho}_{j}, z_{k}) \alpha(\boldsymbol{\rho}_{j}, z_{k}) E^{k}(\boldsymbol{\rho}_{j}, z_{k}).$$
(7

Knowing that each discretization element of the DDA is equivalent to a small sphere of radius  $a=d\sqrt[3]{\frac{3}{4\pi}}$ , the renormalized Born approximation allows us to obtain the exact field in each discretization element within the framework of the static approximation and the Born approximation. This minor

change is interesting as the scattered field no longer increases linearly with the susceptibility. In addition, we use the following polarizability  $\alpha = \alpha_0(1 - (2/3)ik_0^3\alpha_0)$  [23], which introduces the radiation reaction term and energy conservation. We thus expect better behavior of the method when the object contrast increases.

#### C. Vectorial MLB

MLB is easily written for vectorial fields by replacing Green's function with Green's tensor [21]. One obtains

$$\mathbf{E}^{k+1}(\boldsymbol{\rho}_{i}, z_{k+1}) = \mathrm{FFT}_{2D}^{-1} \left[ e^{ik_{z}d} \mathrm{FFT}_{2D} [\mathbf{E}^{k}(z_{k})] \right] (\boldsymbol{\rho}_{i})$$

$$+ \sum_{j} \mathbf{G}(\boldsymbol{\rho}_{i}, z_{k+1}, \boldsymbol{\rho}_{j}, z_{k}) \alpha(\boldsymbol{\rho}_{j}, z_{k}) \mathbf{E}^{k}(\boldsymbol{\rho}_{j}, z_{k}).$$
(8)

Compared to the scalar case, the computation time is three times longer because the three components of the electric field are calculated. Hereafter, we will note VMLB the vectorial MLB.

#### **D. MLB with Reflection**

The main interest of MLB compared to BPM is that it can be easily extended to the calculation of the reflected field [20]. The principle is illustrated in Fig. 3. We still assume that the incident field is a beam propagating toward positive z, but we now consider that the field inside the sample is made of beams propagating in both positive and negative z. For easing the discussion, we note  $E_{+}^{k}(E_{-}^{k})$  the field propagating toward positive (negative) z at layer k. By using Eq. (8), we first calculate the field propagating along the positive z for each layer so that  $E_{+}^{k}$ is known for each k. Then  $E_{-}^{k}$  is assumed to depend only on the field at layer k + 1. At layer K,  $E_{-}^{K}$  is null. Then  $E_{-}^{K-1}$  is set as the field radiated toward negative z by the induced polarization of the Kth layer due to  $E_{+}^{K}$ . At the kth layer,  $E_{-}^{k}$  is written as the sum of the fields radiated toward negative z by the induced polarizations of the k+1 layer due to  $E_+^{k+1}+E_-^{k+1}$  and the field  $E_{-}^{k+1}$  that has undergone free-space propagation of  $z_{k+1}$  to  $z_k$ . Finally, the field at layer k propagating toward negative z is written as

$$\begin{split} \mathbf{E}_{-}^{k}(\boldsymbol{\rho}_{i}, z_{k}) &= \mathrm{FFT}_{2D}^{-1} \left[ e^{-ik_{z}d} \mathrm{FFT}_{2D} [\mathbf{E}_{-}^{k+1}(z_{k+1})] \right] (\boldsymbol{\rho}_{i}) \\ &+ \sum_{j} \mathbf{G}(\boldsymbol{\rho}_{i}, z_{k}, \boldsymbol{\rho}_{j}, z_{k+1}) \alpha(\boldsymbol{\rho}_{j}, z_{k+1}) \\ &\times \left[ \mathbf{E}_{-}^{k+1}(\boldsymbol{\rho}_{j}, z_{k+1}) + \mathbf{E}_{+}^{k+1}(\boldsymbol{\rho}_{j}, z_{k+1}) \right]. \end{split} \tag{9}$$

The total field in the object is the sum of the fields propagating toward positive and negative z,  $E_{tot} = E_+ + E_-$ . Once the field inside the object has been obtained, the scattered field is calculated using Eq. (5).

In the following, we add the letter R (reflection) to the acronyms MLB or VMLB to indicate that the field propagating toward negative z is accounted for in the sample (MLBR and VMLBR).

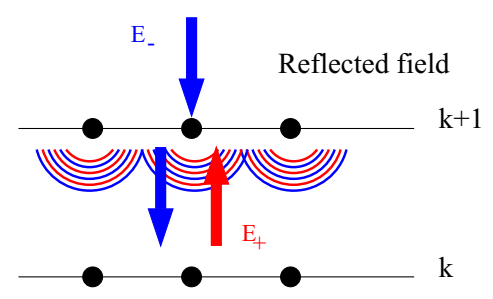


**Fig. 3.** Sketch of the MLB in reflection. The field propagating in  $k_z < 0$  at the layer k is the sum of three components: the field radiated by the dipoles at the layer k+1 due to the field propagating in  $k_z > 0$  (red,  $\mathbf{E}_+$ ); the incident field propagating in  $k_z < 0$  (blue,  $\mathbf{E}_-$ ), and the field radiated by the dipoles at the layer k+1 due to this incident field (circle in blue).

### 4. RESULTS

To study the validity of the different models, we compare the different versions of the MLB with the rigorous calculation obtained by the DDA [13]. We estimate the error for the near field inside the object with

$$\operatorname{Err}_{\mathrm{nf}} = \frac{\int_{V_{\mathrm{obj}}} \|\mathbf{E}_{\mathrm{rig}}(\mathbf{r}) - \mathbf{E}_{\mathrm{approx}}(\mathbf{r})\| \, \mathrm{d}\mathbf{r}}{\int_{V_{\mathrm{obj}}} \|\mathbf{E}_{\mathrm{rig}}(\mathbf{r})\| \, \mathrm{d}\mathbf{r}}$$
(10)

and for the far field

$$\operatorname{Err}_{\mathrm{ff}} = \frac{\int_{2\pi} \left\| \mathbf{F}_{\mathrm{rig}}(\mathbf{k}) - \mathbf{F}_{\mathrm{approx}}(\mathbf{k}) \right\| d\Omega}{\int_{2\pi} \left\| \mathbf{F}_{\mathrm{rig}}(\mathbf{k}) \right\| d\Omega}, \tag{11}$$

where the integration is performed over  $2\pi$  sr for  $k_z > 0$  or  $k_z < 0$ . To enable quantitative comparisons, all the approximate methods and DDA use exactly the same discretization mesh.

# 5. BORN APPROXIMATION VERSUS RENORMALIZED BORN APPROXIMATION

To begin with, we show that using the polarizability, Eq. (7), instead of the susceptibility, Eq. (6), to simulate the field radiated by a given layer improves the calculation of the field inside the object with the MLB. We consider a homogeneous cube of side  $a = 4\lambda$  illuminated by a plane wave along the optical axis. In Fig. 4, we plot  $Err_{nf}$  and  $Err_{ff}$  for  $k_z > 0$  versus the relative permittivity of the cube. Both the scalar and vectorial implementations of MLB are studied. We note the BA implementation using the standard Born approximation and the RBA implementation using the renormalized Born approximation. We observe that RBA improves the calculation of the field inside the object for both MLB and VMLB, as shown in Fig. 4(a). The larger the permittivity, the greater the correction provided by the polarizability, and the better the MLB. If we look at the forward scattered field, Fig. 4(b), we can see that the improvement of the field inside the object is also shown in the far field, particularly for the VMLB. In all the configurations we have tested, using RBA always improves the result. Hence, for the remainder of this article, we will only use RBA.

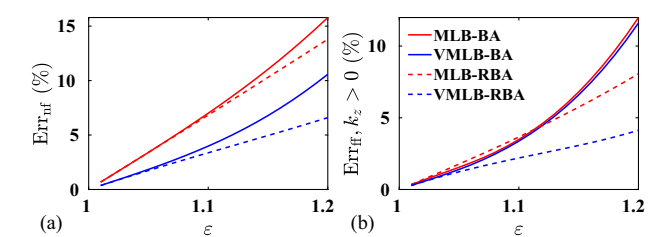


**Fig. 4.** Homogeneous cube of side  $a=4\lambda$  illuminated with a plane wave. (a) Near-field and (b) far-field errors for  $k_z>0$  versus the permittivity.

# 6. COMPARISON OF MLB, VMLB, AND BPM WITH THE RIGOROUS DDA

In this section, we compare the MLB, VMLB, MLBR, and VMLBR with the rigorous DDA for different configurations. We also add the BPM in the comparison, as the latter is close to MLB and requires the same computation time; see Appendix B. We considered the scattering by different objects in air, such as homogeneous or inhomogeneous cuboids or a set of randomly placed spheres. The objects were illuminated by a plane wave propagating along the z axis, except in one case where the plane wave's wave vector made an angle of  $45^{\circ}$  with respect to z. We studied the error behavior as a function of the permittivity of the objects (which was increased moderately).

### A. Cuboid

We first consider a homogeneous cube of side  $4\lambda$  illuminated by a plane wave propagating along z as illustrated in Fig. 5(a). We analyze the near field and far-field errors versus the relative permittivity in Fig. 5. We observe that, for the limited range of permittivity considered, the BPM is equivalent or less accurate than MLB. The salient point of Fig. 5 is to show that the reflected scattered field is significantly better estimated using the VMLBR which takes into account for the vectorial nature of the field and the backpropagated field. For the internal field, the error curves of scalar methods are all merged and increase up to 15% for  $\varepsilon = 1.2$ , see Fig. 5(b), whereas vectorial MLB methods are better by a factor of 2. For the transmitted field, see Fig. 5(d), the MLB methods are slightly better than the BPM, and the VMLB is the best method with an error below 5%.

Surprisingly, while VMLB is significantly more accurate than MLB in near field, the error of VMLB on the backscattered field is similar to MLB. Indeed, the link between near-field and far-field errors is not straightforward. Basically, the nearfield error depends on all the Fourier components of the near field, whereas the far-field error is only related to the Fourier components belonging to a cap of the sphere of the product between near field and susceptibility, as shown in Eq. (5). Now, the near-field Fourier components do not have the same weight. The contribution of the low spatial frequencies is generally dominant in the estimation of the near field. On the other hand, the backscattered field depends mainly on high-frequency components whose weight is negligible in the near-field error. Thus, the good accuracy of VMLB for the near field does not necessarily imply good accuracy for the backscattered field. For estimating the latter, VMLBR is significantly more appropriate than VMLB, as it specifically builds the backpropagating field

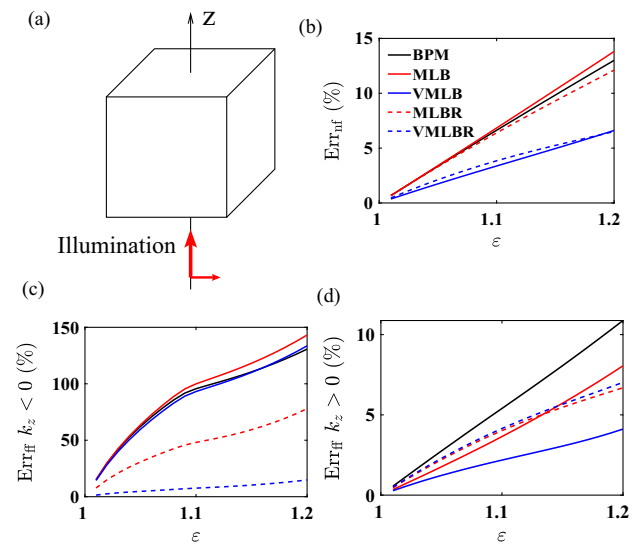


**Fig. 5.** Far-field and near-field relative errors for the different approximate methods under study as a function of the permittivity of the object. (a) The sample is a cube of side  $a=4\lambda$  in air, illuminated by a plane wave along the z axis. (b) Error in near field. (c) Error in far field in reflection ( $k_z < 0$ ). (d) Error in far field in transmission ( $k_z > 0$ ).

at each layer. However, if the forward near field is already well estimated by VMLB or MLB, the inevitable cumulative errors in the backpropagating near field can (marginally) affect the accuracy of the forward diffracted field obtained by radiating the induced polarization.

We have conducted the same analysis by setting the cuboid permittivity to 1.1 and increasing its size from 2 to 15 wavelengths (not shown). We observed the same behavior. The error on the near field and transmitted field increases with the cuboid size but remains smaller than 15% for all the methods. On the other hand, only VLMBR is able to estimate the reflected far field correctly, with an error significantly smaller than 50%. VLMBR error increases from 10% to 30% with the cuboid size, while the errors of the other methods start at 50% and rapidly reach 150%.

The interest of taking into account the backpropagating fields in MLB is also evidenced if one is interested in the internal field inside the sample. We plot in Fig. 6 the modulus of the electric field in the plane (x, z) in the middle of the cube for the rigorous and approximate methods. Clearly, the complex field features are best reproduced using MLBR or VMLBR.

Then the key advantage of accounting for the vectorial nature of the field, VMLBR, is that all the components of the electric field are computed, while the other methods (BPM, MLB, and MLBR) deal with scalar fields. The *y* and *z* components of the field estimated by VMLBR displayed in Fig. 7 show a good agreement with the rigorous DDA.

In Fig. 8(a), we consider the same object under oblique illumination, 45°. This configuration is not adapted to the BPM [36] which provides the worst results. We observe that VMLBR is now significantly better than the other techniques for both the internal, reflected, and transmitted far fields. The influence of the vectorial nature of the field was indeed expected to be enhanced in this "corner cube" configuration. At 45° incidence, the backpropagating field is significantly larger than at normal

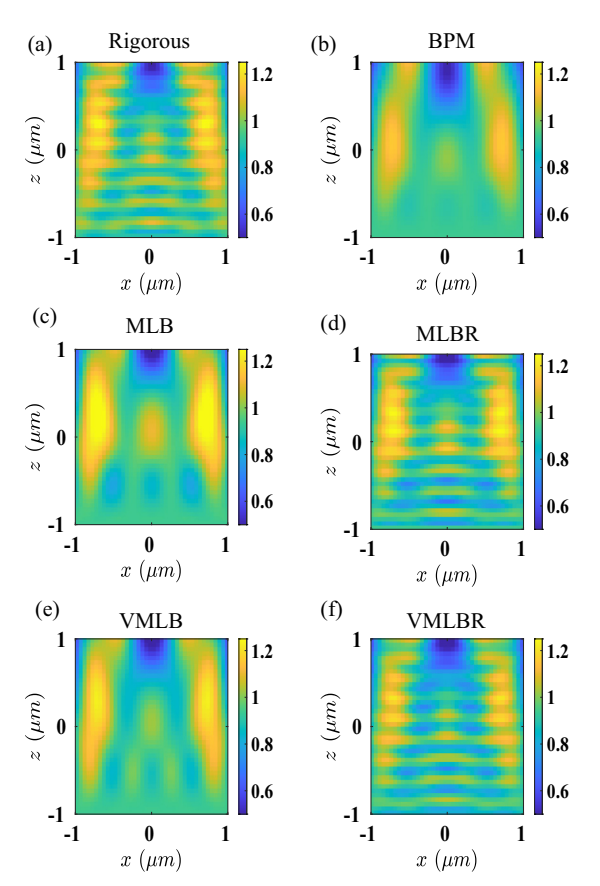


**Fig. 6.** Modulus of the field inside the cube at y = 0 for  $\varepsilon = 1.2$ . (a) Rigorous. (b) BPM. (c) MLB. (d) MLBR. (e) VMLB. (f) VMLBR.

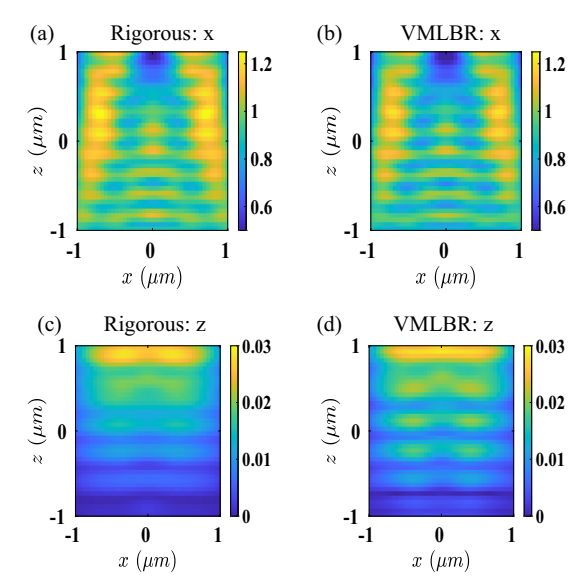


**Fig. 7.** Modulus of the field inside the cube at y = 0 and  $\varepsilon = 1.2$  for the y and z components with the DDA and the VMLBR.

incidence (the interference fringes in the near field for VMLBR are more contrasted at 45° than at 0°; see Fig. 6). It cannot be neglected when radiating the induced polarization. In this case, the VMLBR performs better than all the other methods for the near field and both forward and backward scattered far fields.

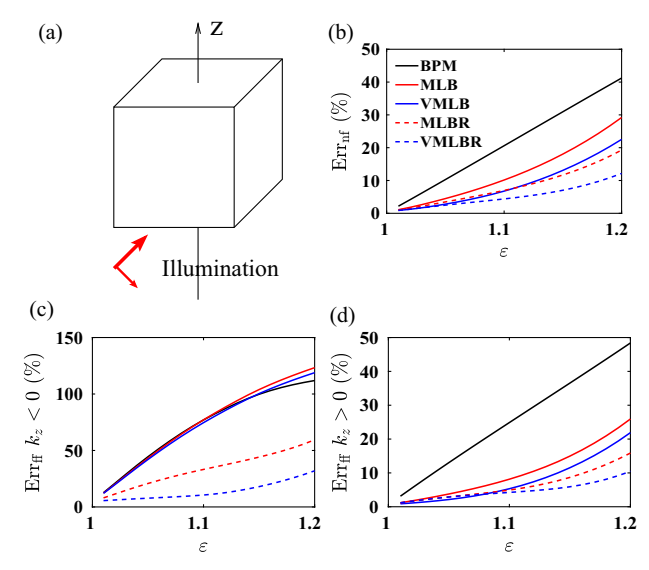


**Fig. 8.** Same as Fig. 5 except that the cube is now illuminated with a plane wave at  $45^{\circ}$  of the z axis.

# **B.** Inhomogeneous Object

We now consider a weakly contrasted random inhomogeneous medium illuminated by a plane wave propagating along the z axis to better approximate a biological sample in a tomography setup. We consider a cuboid of permittivity a Gaussian-distributed random variable of mean  $\varepsilon_{\rm bg}$  and variance  $\sigma^2$ , with a Gaussian correlation function [37]:  $\langle \varepsilon({\bf r}), \varepsilon({\bf r}') \rangle = \varepsilon_{\rm bg}^2 + \sigma^2 \exp(-\frac{\|{\bf r}-{\bf r}'\|^2}{l_c^2})$ , embedded into a homogeneous background of permittivity  $\varepsilon_{\rm bg}$ . The relative errors for the far and near fields for a cube of  $L=60\lambda$  are shown in Figs.  $9({\rm a})-9({\rm c})$  as a function of the permittivity standard deviation  $\sigma$ . At low  $\sigma$ , all methods behave in a similar way for estimating the transmitted far field, while VMLBR is more accurate for estimating the reflected far field. At high  $\sigma$ , the reflected far field is badly estimated, whatever the methods, with a better robustness of BPM.

In Figs. 9(d)–9(f), the object under study is a cuboid of size  $(40\lambda)^2 \times L$  with  $l_c = \lambda$  and  $\sigma = 0.01$ . We study the error as a function of sample thickness L. In this configuration, at low  $\sigma$ , the VLMBR is significantly better than the other methods for estimating the reflected far field whatever L.

Note that for the field inside the object, the VLMB(R) is always the best method, whatever the configuration studied; see Figs. 9(a) and 9(d).

### C. Multiple Beads

In the last configuration, we consider an extended sample with sharp transitions between the background and spherical inclusions with quite a large size. We study a random distribution of beads of radius  $r=2\lambda$  in a cube of side  $80\lambda$ , where the fraction of volume occupied by the spheres in the cuboid is 0.05 (763 beads). The mesh size is  $\lambda/5$  yielding  $N=400^3=64\times10^6$  subunits. We observe in Fig. 10 that the methods are roughly equivalent except for the reflected far field where VMLBR stands out clearly as the best technique.

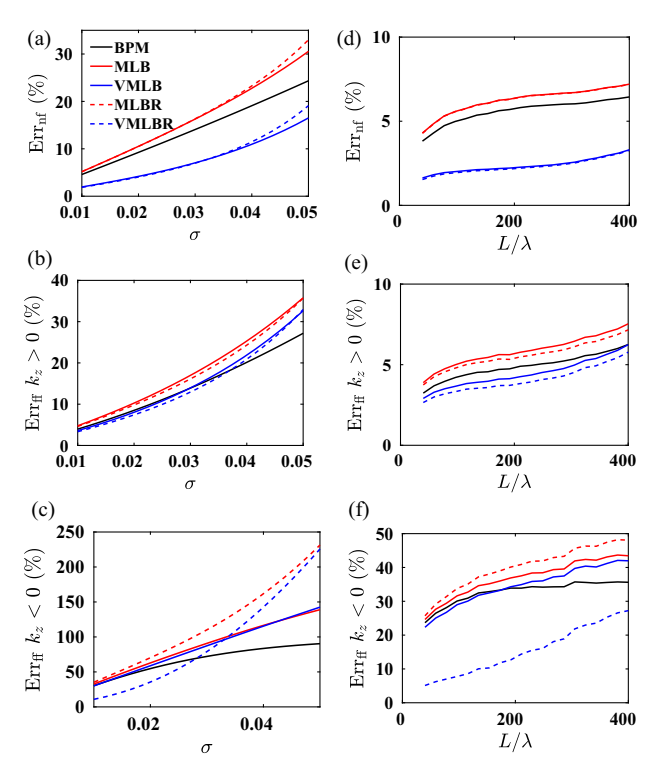


**Fig. 9.** Far-field and near-field relative errors for a random medium as a function of the permittivity standard deviation  $\sigma$  (a, c) or thickness of the medium L (b, d). (a)–(c) The sample is a random inhomogeneous cuboid of size  $60\lambda \times 60\lambda \times 60\lambda$  with permittivity correlation length  $l_c = \lambda$ . (d)–(f) The sample is an inhomogeneous cuboid of size  $40\lambda \times 40\lambda \times L$  with  $l_c = \lambda$  and  $\sigma = 0.01$ .

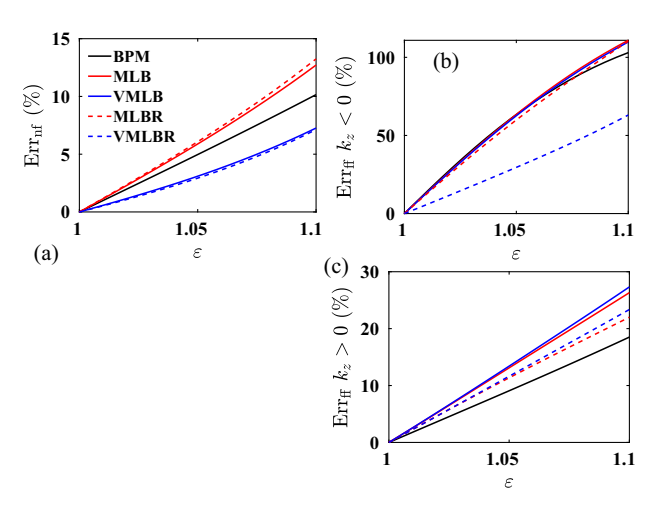


**Fig. 10.** Far-field and near-field relative errors as a function of the permittivity of randomly placed beads within a cube of side 80 $\lambda$ . The radius of the beads is  $r = 2\lambda$ ; their volume fraction is 0.05.

In Fig. 11, we compare the computation time of the different MLB techniques and the rigorous calculation of DDA, for the object presented in Fig. 10, as a function of the permittivity contrast. We observe in Fig. 11 that, as expected, the computation time of MLB techniques does not depend on the dielectric contrast of the sample (except for some fluctuations due to the processors communication and system load). On the contrary, the computation time of DDA increases significantly with

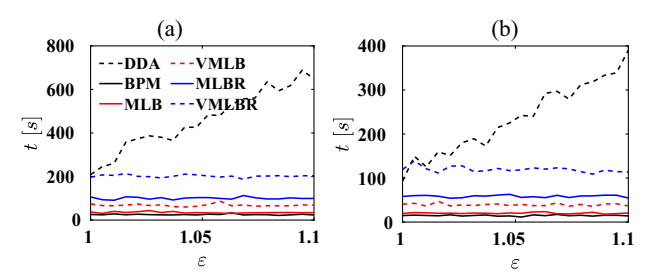


**Fig. 11.** Time of computation for the object presented in Fig. 10.

the permittivity contrast because the solving of its linear system requires more iterations. Unsurprisingly, the refinements brought to MLB (backpropagation, vectorial nature of the fields) increase the computation cost: VMLBR is about 10 times slower than the scalar MLB. At a small permittivity contrast, the computation time of VMLBR is close to that of DDA. In this case, the solving of the linear system in DDA requires very few iterations that are performed with 3D fast Fourier transforms whose support is limited to the object support. For their part, the 2D FFTs involved in the MLB have a significantly larger size than the object support to avoid aliasing and are less efficiently parallelized than the 3D ones of DDA.

Note that DDA computation time could be reduced by accepting some inaccuracy in the solving of its linear system (increasing the tolerance threshold) or by taking appropriate initial guess as in Refs. [29,38].

### 7. CONCLUSION

To conclude, we have demonstrated that the multilayer Born model accounting for the vectorial nature of the field and the backpropagated beam (VMLBR) was significantly more efficient than BPM or standard MLB for estimating the reflected far field and comparable to the latter for estimating the transmitted far field. Its validity domain is similar to that of standard MLB: permittivity contrast smaller than 0.2 and sample thickness about tens of  $\lambda$ .

The computation time of VMLBR is about 10 times longer than that of BPM, as illustrated in Fig. 11. It can be close to that of DDA for very small permittivity contrast (when multiple scattering is limited).

In our opinion, VMLBR is mainly of interest for reflective configurations and for samples that supports only moderate multiple scattering. It can easily be extended to anisotropic material [21].

# APPENDIX A: DETAILS ON THE IMPLEMENTATION OF THE MLB

This appendix details the implementation of MLB [Eq. (6)] and others. The computation of the second term  $FFT_{2D}^{-1}[e^{ik_zd}FFT_{2D}[E^k(z_k)]](\boldsymbol{\rho}_i)$  of Eq. (6) is similar to that of the BPM. To avoid edge effects and aliasing, the size of the FFT shall be slightly larger than the support of  $\chi$ . The other term,

$$\sum_{i} G(\boldsymbol{\rho}_{i}, z_{k+1}, \boldsymbol{\rho}_{j}, z_{k}) \chi(\boldsymbol{\rho}_{j}, z_{k}) d^{3} E^{k}(\boldsymbol{\rho}_{j}, z_{k}), \quad \text{(A1)}$$

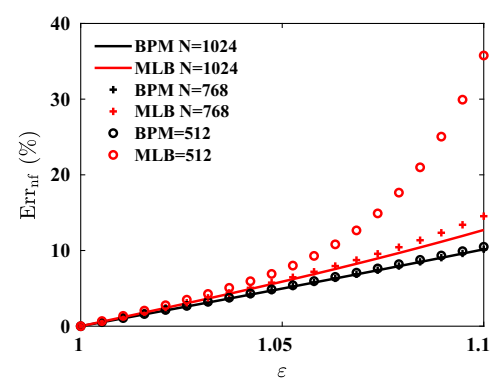


**Fig. 12.** Study of convergence of the MLB and BPM. Near-field error versus  $\varepsilon$  for different size of FFT for the object presented in Fig. 10.

is also computed using FFT in the (x, y) plane due to translational invariance [39,40]. The size of the FFT is taken large enough to avoid the edge effects caused by the slow decay of the Green function. In this case, we observed that it had to be significantly larger than the support of  $\chi$ . In Fig. 12, with the object of Section 6.C, we show the error between DDA, MLB, and BPM for different FFT sizes. The object presented in Section 6.C has a number of subunits in the (x, y) plane of  $400 \times 400$ , and it is necessary to take an FFT of at least  $1024 \times 1024$  for the MLB to get a converged result. For the BPM, on the other hand, the FFT size is less critical, and 512 is sufficient. This is due to the fact that Green's function decreases slowly in 1/r, which requires a larger FFT size, especially as the object has a high permittivity.

# APPENDIX B: THEORETICAL COMPARISON BETWEEN MLB AND BPM

In this appendix, we show that under the paraxial approximation, MLB and BPM expressions are similar in the limit of small refractive index contrasts. BPM divides the object into layers perpendicular to the optical axis. The field in a given layer is obtained from the one in the previous layer through the relation [111].

$$E^{k+1}(\boldsymbol{\rho}_{i}, z_{k+1}) = \text{FFT}_{2D}^{-1} \left[ e^{ik_{z}d} \text{FFT}_{2D} \left[ e^{ik_{0}\Delta n(z_{k})d} E^{k}(z_{k}) \right] \right] (\boldsymbol{\rho}_{i}),$$
**(B1**)

where  $\Delta n(\mathbf{r})$  is the refractive index contrast of the object. When the contrast is weak, the exponential can be expanded in a Taylor series to first order, yielding,

$$\begin{split} E^{k+1}(\boldsymbol{\rho}_i, \, z_{k+1}) &= \mathrm{FFT}_{2D}^{-1} \left[ e^{ik_z d} \mathrm{FFT}_{2D} [E^k(z_k)] \right] (\boldsymbol{\rho}_i) \\ &+ ik_0 d \mathrm{FFT}_{2D}^{-1} \left[ e^{ik_z d} \mathrm{FFT}_{2D} [\Delta n(z_k) E^k(z_k)] \right] (\boldsymbol{\rho}_i). \end{split}$$

We now rewrite the MLB equation, Eq. (6), under the paraxial approximation. The scalar free-space Green's function can be reformulated by the plane wave expansion as follows [41]:

$$G(\mathbf{r}, \mathbf{r}') = k_0^2 \iint \frac{i}{2\pi k_z} e^{i\kappa \cdot (\rho - \rho')} e^{ik_z|z - z'|} d\kappa, \qquad (B3)$$

where  $\kappa = (k_x, k_y)$  is the 2D transverse component of wave vectors. We obtain

$$G(\boldsymbol{\rho}_i, z_{k+1}, \boldsymbol{\rho}_j, z_k) = \frac{ik_0}{2\pi} \iint e^{i\boldsymbol{\kappa}\cdot(\boldsymbol{\rho}_i - \boldsymbol{\rho}_j)} e^{ik_z d} d\boldsymbol{\kappa}.$$
 (B4)

If we now assume that the object refractive index varies weakly about 1, we obtain  $\chi(\boldsymbol{\rho}_j,z_k)=\frac{n^2(\boldsymbol{\rho}_j,z_k)-1}{4\pi}\simeq\frac{\Delta n(\boldsymbol{\rho}_j,z_k)}{2\pi}$ . In this case, the scattered field by the layer k at k+1, Eq. (6), can be rewritten as

$$\begin{split} E_s^{k+1}(\boldsymbol{\rho}_i, z_{k+1}) \\ &= \sum_j G(\boldsymbol{\rho}_i, z_{k+1}, \boldsymbol{\rho}_j, z_k) \chi(\boldsymbol{\rho}_j, z_k) d^3 E^k(\boldsymbol{\rho}_j, z_k) \\ &= \frac{ik_0}{4\pi^2} \sum_j \left( \iint e^{i\kappa \cdot (\boldsymbol{\rho}_i - \boldsymbol{\rho}_j)} e^{ik_z d} d\kappa \right) \Delta n(\boldsymbol{\rho}_j, z_k) d^3 E^k(\boldsymbol{\rho}_j, z_k) \\ &= \frac{ik_0 d}{4\pi^2} \iint \left( \sum_i \Delta n(\boldsymbol{\rho}_j, z_k) E^k(\boldsymbol{\rho}_j, z_k) e^{-i\kappa \cdot \boldsymbol{\rho}_j} d^2 \right) e^{ik_z d} e^{i\kappa \cdot \boldsymbol{\rho}_i} d\kappa \end{split}$$

$$=ik_0d\mathrm{FFT}_{2D}^{-1}\left[e^{ik_zd}\mathrm{FFT}_{2D}[\Delta n(z_k)E^k(z_k)]\right](\boldsymbol{\rho}_i).$$
**(B5)**

By adding to the scattered field, Eq. (B5), the incident field that propagates from layer k to k+1, i.e.,  ${\rm FFT}_{2D}^{-1}[e^{ik_zd}{\rm FFT}_{2D}[E^k(z_k)]](\boldsymbol{\rho}_i)$ , we recover the same expression as Eq. (B2). We have shown that for weakly contrasted objects and under the paraxial approximation, BPM and MLB are actually the same methods.

**Disclosures.** The authors declare no conflicts of interest.

**Data availability.** Data underlying the results presented in this paper are not publicly available at this time, but the IFDDA code under free license is available at Ref. [30] and allows one to redo all the calculations presented in this article.

# **REFERENCES**

- S. Molesky, Z. Lin, A. Y. Piggott, et al., "Inverse design in nanophotonics," Nat. Photonics 12, 659–670 (2018).
- M. Lee, H. Hugonnet, and Y. Park, "Inverse problem solver for multiple light scattering using modified Born series," Optica 9, 177–182 (2022).
- C. Godavarthi, T. Zhang, G. Maire, et al., "Superresolution with full-polarized tomographic diffractive microscopy," J. Opt. Soc. Am. A 32, 287–292 (2015).
- U. S. Kamilov, I. N. Papadopoulos, M. H. Shoreh, et al., "Learning approach to optical tomography," Optica 2, 517–522 (2015).
- H.-Y. Liu, D. Liu, H. Mansour, et al., "SEAGLE: sparsity-driven image reconstruction under multiple scattering," IEEE Trans. Comput. Imaging 4, 73–86 (2018).
- J. Zhu, H. Wang, and L. Tian, "High-fidelity intensity diffraction tomography with a non-paraxial multiple-scattering model," Opt Express 30, 32808–32821 (2022).
- S. Moser, A. Jesacher, and M. Ritsch-Marte, "Efficient and accurate intensity diffraction tomography of multiple-scattering samples," Opt. Express 31, 18274–18289 (2023).
- 8. T. M. Habashy, R. W. Groom, and B. R. Spies, "Beyond the Born and Rytov approximations: a nonlinear approach to electromagnetic scattering," J. Geophys. Res.-Solid Earth 98, 1759–1775 (1993).
- R. Carminati, "Phase properties of the optical near field," Phys. Rev. E 55, R4901–R4904 (1997).
- B. Chen and J. J. Stamnes, "Validity of diffraction tomography based on the first Born and the first Rytov approximations," Appl. Opt. 37, 2996–3006 (1998).

- U. S. Kamilov, I. N. Papadopoulos, M. H. Shoreh, et al., "Optical tomographic image reconstruction based on beam propagation and sparse regularization," IEEE Trans. Comput. Imaging 2, 59–70 (2016).
- J. V. Roey, J. van der Donk, and P. E. Lagasse, "Beam-propagation method: analysis and assessment," J. Opt. Soc. Am. 71, 803–810 (1981).
- P. C. Chaumet, "The discrete dipole approximation: a review," Mathematics 10, 3049 (2022).
- P. C. Chaumet, A. Sentenac, and T. Zhang, "Reflection and transmission by large inhomogeneous media. Validity of Born, Rytov and beam propagation methods," J. Quant. Spectrosc. Radiat. Transfer 243, 106816 (2020).
- A. Badon, D. Li, G. Lerosey, et al., "Smart optical coherence tomography for ultra-deep imaging through highly scattering media," Sci. Adv. 2, e1600370 (2016).
- E. Mudry, P. C. Chaumet, K. Belkebir, et al., "Electromagnetic wave imaging of three-dimensional targets using a hybrid iterative inversion method," Inverse Probl. 28, 065007 (2012).
- T. Zhang, Y. Ruan, G. Maire, et al., "Full-polarized tomographic diffraction microscopy achieves a resolution about one-fourth of the wavelength," Phys. Rev. Lett. 111, 243904 (2013).
- S. Kang, S. Jeong, W. Choi, et al., "Imaging deep within a scattering medium using collective accumulation of single-scattered waves," Nat. Photonics 9, 253–258 (2015).
- A. Matlock, A. Sentenac, P. C. Chaumet, et al., "Inverse scattering for reflection intensity phase microscopy," Biomed. Opt. Express 11, 911–926 (2020).
- M. Chen, D. Ren, H.-Y. Liu, et al., "Multi-layer Born multiplescattering model for 3D phase microscopy," Optica 7, 394–403 (2020).
- S. Mu, Y. Shi, Y. Song, et al., "Multislice computational model for birefringent scattering," Optica 10, 81–89 (2023).
- E. M. Purcell and C. R. Pennypacker, "Scattering and absorption of light by nonspherical dielectric grains," Astrophys. J. 186, 705–714 (1973)
- B. T. Draine, "The discrete-dipole approximation and its application to interstellar graphite grains," Astrophys. J. 333, 848–872 (1988).
- M. A. Yurkin and A. G. Hoekstra, "The discrete dipole approximation: an overview and recent developments," J. Quant. Spect. Rad. Transf. 106, 558–589 (2007).
- 25. J. D. Jackson, Classical Electrodynamics, 2nd ed. (Wiley, 1975).
- A. D. Yaghjian, "Electric dyadic Green's functions in the source region," Proc. IEEE 68, 248–263 (1980).
- P. C. Chaumet, A. Sentenac, and A. Rahmani, "Coupled dipole method for scatterers with large permittivity," Phys. Rev. E 70, 036606 (2004).
- P. C. Chaumet and A. Rahmani, "Efficient iterative solution of the discrete dipole approximation for magneto-dielectric scatterers," Opt. Lett. 34, 917–919 (2009).
- P. C. Chaumet, G. Maire, and A. Sentenac, "Accelerating the discrete dipole approximation by initializing with a scalar solution and using a circulant preconditioning," J. Quant. Spectrosc. Radiat. Transfer 298, 108505 (2023).
- 30. P. C. Chaumet, A. Sentenac, and D. Sentenac, "Software IFDDA and IFDDAM," https://www.fresnel.fr/perso/chaumet/ifdda.html.
- A. Lakhtakia, "General theory of the Purcell-Pennypacker scattering approach and its extension to bianisotropic scatterers," Astrophys. J. 394, 494–499 (1992).
- B. T. Draine and J. Goodman, "Beyond Clausius-Mossotti: wave propagation on a polarizable point lattice and the discrete dipole approximation," Astrophys. J. 405, 685–697 (1993).
- K. Belkebir, P. C. Chaumet, and A. Sentenac, "Superresolution in total internal reflection tomography," J. Opt. Soc. Am. A 22, 1889–1897 (2005).
- P. C. Chaumet, T. Zhang, and A. Sentenac, "Fast far-field calculation in the discrete dipole approximation," J. Quant. Spectrosc. Radiat. Transfer 165, 88–92 (2015).
- P. C. Chaumet, G. Maire, and A. Sentenac, "Scalar approximation of Maxwell equations: derivation and accuracy," J. Opt. Soc. Am. A 39, 1462–1467 (2022).
- G. R. Hadley, "Multistep method for wide-angle beam propagation," Opt. Lett. 17, 1743–1745 (1992).

- T. Zhang, P. C. Chaumet, E. Mudry, et al., "Electromagnetic wave imaging of targets buried in a cluttered medium using a hybrid inversion-DORT method," Inverse Probl. 28, 125008 (2012).
- K. G. Inzhevatkin and M. A. Yurkin, "Uniform-over-size approximation of the internal fields for scatterers with low refractive-index contrast," J. Quant. Spectrosc. Radiat. Transfer 277, 107965 (2022).
- 39. P. J. Flatau, G. L. Stephens, and B. T. Draine, "Light scattering by rectangular solids in the discrete-dipole approximation: a new algo-
- rithm exploiting the Block-Toeplitz structure," J. Opt. Soc. Am. A 7, 593–600 (1990).
- J. Goodman and P. J. Flatau, "Application of fast-Fourier-transform techniques to the discrete-dipole approximation," Opt. Lett. 16, 1198–1200 (2002).
- 41. M. Born and E. Wolf, *Principles of Optics* (Cambridge University, 1999).